Cold dilute neutron matter on the lattice. I. Lattice virial coefficients and large scattering lengths

Dean Lee and Thomas Schäfer
Department of Physics, North Carolina State University, Raleigh, North Carolina 27695, USA
(Received 20 September 2005; published 13 January 2006)

We study cold dilute neutron matter on the lattice using an effective field theory. We work in the unitary limit in which the scattering length is much larger than the interparticle spacing. In this article we focus on the equation of state at temperatures above the Fermi temperature and compare lattice simulations to the virial expansion on the lattice and in the continuum. We find that in the unitary limit lattice discretization errors in the second virial coefficient are significantly enhanced. As a consequence the equation of state does not show the universal scaling behavior expected in the unitary limit. We suggest that scaling can be improved by tuning the second virial coefficient rather than the scattering length.

DOI: 10.1103/PhysRevC.73.015201 PACS number(s): 24.85.+p, 21.30.−x, 13.75.Cs, 21.65.+f

I. INTRODUCTION

Cold dilute neutron matter is an intriguing physical system. It is relevant to the physics of the inner crust of neutron stars [1]. It is also close to an interesting universal limit that is the result of a large separation of scales. The neutron scattering length is $a_{nn} \simeq -18$ fm, which implies that the dimensionless parameter $k_F|a_{nn}| \gg 1$ for densities $\rho > 10^{-4}\rho_N$. Here, $k_F = (3\pi^2\rho)^{1/3}$ is the Fermi momentum and $\rho_N \simeq 0.16$ fm^{-3} is the saturation density of nuclear matter. The effective range, however, is $r_{nn} \simeq 2.8$ fm. So if the density is very small, $\rho < 0.1\rho_N$, then $k_F|r_{nn}|$ is a small parameter and neutron matter is close to the limit in which $k_F|a_{nn}| \to \infty$ and $k_F|r_{nn}| \to 0$. This is known as the unitary limit, where the vacuum scattering amplitude in the s-wave channel has a zero-energy resonance, and the cross-section saturates the unitarity bound. In this limit there is no expansion parameter and the calculation of the equation of state and of transport properties is a difficult nonperturbative problem. It is now possible to create systems of fermions in the unitary limit in the laboratory by trapping fermionic atoms and tuning the scattering length using a Feshbach resonance [2–6]. This technique will provide experimental measurements of universal parameters, but it is clearly desirable to also develop a computational approach. There are several computational studies of neutron matter at zero temperature using potential models and Green's function Monte Carlo [7–10]. Recently, there have also been simulations on the lattice using effective field theory [11–18]. The main advantage of the effective field theory/lattice approach for the dilute neutron matter problem is that it is not restricted to zero temperature.

We have described our method and some initial results in Ref. [15]. This is the first in a sequence of two articles in which we perform a careful study of the parameter dependence and scaling behavior of the results. We are particularly interested in verifying that the lattice results satisfy the scaling relations that are expected to hold in the unitary limit. The main focus of this first article is to understand the equation of state at low density and temperature higher than the Fermi energy and compare the results to the virial expansion. We find that if the scattering length is large lattice discretization errors can be as large as 100% or more. At fixed lattice spacing when the temperature decreases we find that the error first increases before eventually decreasing. To counter this effect, we propose that the interaction coefficient be tuned to give the correct second-order virial coefficient, $b_2(T)$, at the chosen simulation temperature. We describe in detail how this is done. In the sequel to this article we apply this technique to simulations of cold dilute neutron matter in the unitary limit and study the scaling behavior of the results.

II. LATTICE ACTION

We consider the theory defined by the partition function

$$Z_G = Tr\exp[-\beta(H-\mu N)] \simeq z_0 e^{2\mu\beta L^3} \times \int Ds\, Dc'\, Dc^* \exp[-S]\,, \tag{1}$$

where the lattice action is given by the following:

$$S = \sum_{\vec{n},i}[e^{-\mu\alpha_t}c_i^*(\vec{n})c_i'(\vec{n}+\hat{0}) - e^{\sqrt{-C\alpha_t}s(\vec{n})+\frac{C\alpha_t}{2}} \times (1-6h)c_i^*(\vec{n})c_i'(\vec{n})] - h\sum_{\vec{n},l_s,i}[c_i^*(\vec{n})c_i'(\vec{n}+\hat{l}_s) + c_i^*(\vec{n})c_i'(\vec{n}-\hat{l}_s)] + \frac{1}{2}\sum_{\vec{n}} s^2(\vec{n}). \tag{2}$$

Here, $\vec{n}$ labels the sites of a 3+1 dimensional lattice, $\hat{l}_s (s = 1, 2, 3)$ is a spatial unit vector, and i labels the two spin components of the neutron, $\uparrow$ and $\downarrow$. The spatial lattice spacing is a and $\alpha_t = a_t/a$ is the ratio of the temporal to the spatial lattice spacing. The spatial volume of the lattice is L^3 and the temporal length is $\beta = 1/T$. Dimensional quantities such as the chemical potential μ and the nucleon mass m_N are given in units of the lattice spacing a. We have also defined $h = \alpha_t/(2m_N)$. The Grassmann fields are denoted by $c_i(\vec{n})$ and $s(\vec{n})$ is a Hubbard-Stratonovich field.

The interaction coefficient C must be determined for given lattice spacings a and a_t. In Ref. [15] this was done by adjusting C to reproduce the correct neutron scattering length at zero

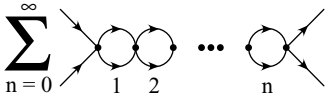

FIG. 1. Diagrams contributing to neutron-neutron scattering.

temperature. This requires summing the two-particle scattering diagrams shown in Fig. 1. The pole in the scattering amplitude is then compared with Lüscher's formula for energy levels in a finite periodic box [19,20],

$$E_0 = \frac{4\pi a_{\rm scatt}}{m_N L^3}\left[1 - c_1\frac{a_{\rm scatt}}{L} + c_2\frac{a_{\rm scatt}^2}{L^2} + \cdots\right], \qquad (3)$$

where $c_1 = -2.837297$, $c_2 = 6.375183$.

III. RESULTS FOR LARGE SCATTERING LENGTHS

We present lattice simulation results for the energy per particle as a function of density for several different scattering lengths. We are interested in cold dilute neutron matter where all length scales are much larger than the lattice spacing. We use a spatial lattice spacing of $a = (50\ {\rm MeV})^{-1}$ and temporal lattice spacing of $a_t = (24\ {\rm MeV})^{-1}$. We consider scattering lengths $|a_{\rm scatt}| > 4.675$ fm. The spatial lattice spacing was chosen so that it is smaller than the smallest scattering length. The temporal lattice spacing was chosen sufficiently small so that the results are very close to the $a_t \to 0$ limit. We have computed the energy per neutron for five different scattering lengths. The corresponding operator coefficients are shown in Table I.

We have also shown the derivative $dC/d\alpha_t$ that is needed to compute derivatives with respect to β.

We use the hybrid Monte Carlo algorithm [21] to generate Hubbard-Stratonovich field configurations as described in Ref. [15]. We use diagonal preconditioning before each conjugate gradient solve. If K is the single-spin neutron matrix for a given Hubbard-Stratonovich field configuration, then we must solve the linear equation

$$K^\dagger K v = b. \qquad (4)$$

Rather than solving this directly, we make use of the diagonal matrix

$$D = {\rm diag}[K^\dagger K] \qquad (5)$$

and solve instead

$$[D^{-1}K^\dagger K D^{-1}]Dv = D^{-1}b. \qquad (6)$$

Fluctuations associated with the Hubbard-Stratonovich field occur on the diagonal of K, and therefore the matrix $D^{-1}K^\dagger K D^{-1}$ typically has a smaller condition number than

TABLE I. Operator coefficients and scattering lengths.

$C\,(10^{-4}\,{\rm MeV}^{-2})$	-1.028	-1.108	-1.153	-1.257	-1.318
$dC/d\alpha_t\,(10^{-5}\,{\rm MeV}^{-2})$	-2.259	-2.239	-2.218	-2.141	-2.078
$a_{\rm scatt}$ (fm)	-4.675	-9.35	-18.70	$+18.70$	$+9.35$

TABLE II. L dependence for $a_{\rm scatt} = -18.70$ fm, $T = 4$ MeV, $\mu = 0$.

L	$\rho^{\rm bubble}\,(10^{-3}\,{\rm fm}^{-3})$	$\frac{E^{\rm bubble}}{A^{\rm bubble}}$(MeV)	$\rho^{\rm sim}\,(10^{-3}\,{\rm fm}^{-3})$	$\frac{E^{\rm sim}}{A^{\rm sim}}$(MeV)
4	7.688	3.527	8.70(3)	3.41(3)
5	7.695	3.521	8.78(10)	3.41(3)
6	7.695	3.521	8.81(10)	3.39(3)

$K^\dagger K$. We further improve the performance by adding a small positive constant ϵ to produce the modified equation

$$[D^{-1}K^\dagger K D^{-1} + \epsilon]Dv = D^{-1}b. \qquad (7)$$

We tune ϵ so that the equilibration time for the hybrid Monte Carlo algorithm is minimized while keeping the induced systematic error smaller than the stochastic error. In practice we take ϵ to be 10^{-4} or smaller.

Roughly 10^4 HMC trajectories were run, split across four processors running completely independent trajectories. Averages and errors were computed by comparing the results of each processor. The finite volume error was tested by going to larger volumes. The final lattice sizes were chosen so that the finite volume error was less than 1%. For the data at $T = 4$ MeV we used a lattice of size $4^3 \times 6$. For $T = 3$ MeV we used $5^3 \times 8$, and for $T = 2$ MeV we used $5^3 \times 12$. As an example of the finite volume dependence, we show in Table II the density and energy per particle from simulations with lattice volumes $4^3, 5^3, 6^3$ at $a_{\rm scatt} = -18.70$ fm, $T = 4$ MeV, and $\mu = 0$. For comparison we also show the volume dependence of the bubble chain calculations described in Ref. [15] and Sec. V.

These results suggest that the finite volume effects are smaller than the statistical errors. If we take the volume dependence from the bubble chain calculations as a guide, then the finite volume errors are well below 1%.

Figure 2 shows the lattice simulation results for the energy per neutron at $T = 4$ MeV. Figure 3 shows the energy per neutron at $T = 3$ MeV, and Fig. 4 shows the energy per

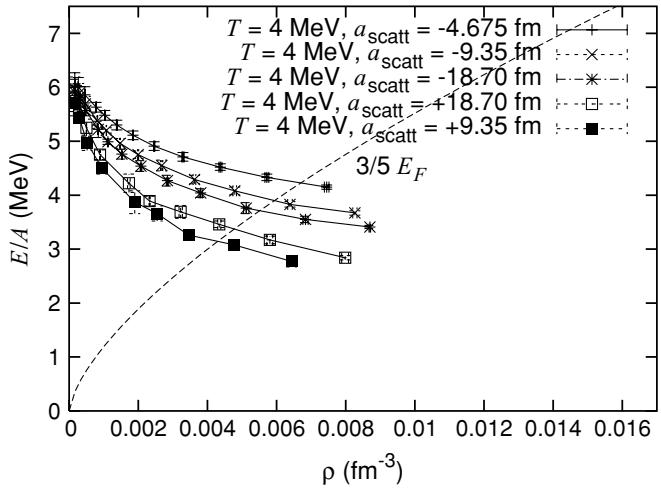

FIG. 2. Energy per neutron versus density at $T = 4$ MeV for various scattering lengths.

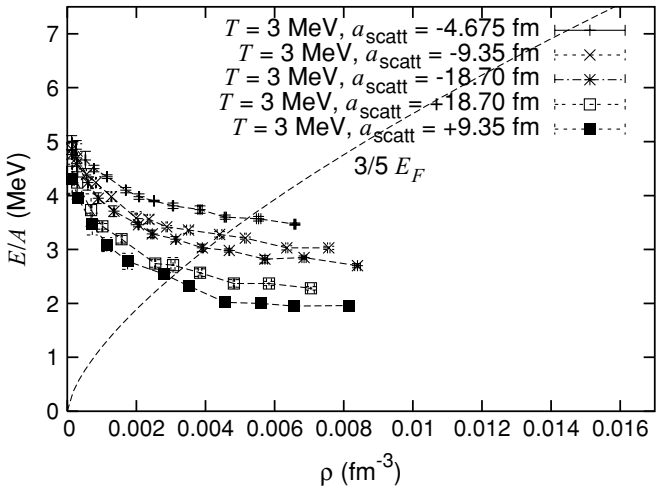

FIG. 3. Energy per neutron versus density at $T = 3$ MeV for various scattering lengths.

neutron at $T = 2$ MeV. In each of the plots we have taken a range of densities from zero to a quarter-filled lattice. With a spatial lattice spacing of $(50\ \text{MeV})^{-1}$, the quarter-filled lattice corresponds with a density of $0.0081\ \text{fm}^{-3}$. Beyond this one might find significant lattice artifacts. We observe that the energy per particle depends quite strongly on the scattering length, both at large and at small density. Although the dependence of E/A on the scattering length for a degenerate Fermi gas is a complicated, nonperturbative problem it is possible to compare our results to theoretical predictions in the opposite limit of low density and temperature higher than the Fermi energy.

IV. VIRIAL EXPANSION

The virial expansion arranges multiparticle interactions as a power series in fugacity,

$$z = e^{\beta\mu}. \tag{8}$$

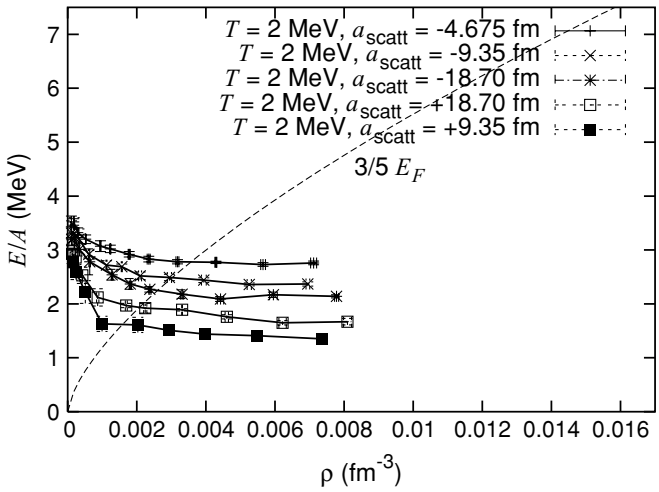

FIG. 4. Energy per neutron versus density at $T = 2$ MeV for various scattering lengths.

For example, the logarithm of the partition function per unit volume can be written as follows,

$$\frac{1}{V}\ln Z_G = \beta P = \frac{2}{\lambda_T^3}[z + b_2(T)z^2 + b_3(T)z^3\cdots]. \tag{9}$$

The second-order virial coefficient $b_2(T)$ is determined entirely by two-particle interactions, whereas the third virial coefficient depends on three-body interactions, and so on. We can use the virial expansion to compute thermodynamic observables in the high-temperature/low-density limit. The virial expansion is reliable if the thermal wavelength $\lambda_T = \sqrt{(2\pi)/(m_N T)}$ is smaller than the interparticle spacing, $\lambda_T < \rho^{-1/3}$. The neutron density can be computed in terms of the derivative of $\ln Z_G$ with respect to the chemical potential,

$$\rho = \frac{A}{V} = \frac{1}{\beta V}\frac{\partial}{\partial\mu}\ln Z_G. \tag{10}$$

To second order in the virial expansion we find

$$\rho = \frac{2}{\lambda_T^3}[z + 2b_2(T)z^2 + \cdots]. \tag{11}$$

As a result of discretization error we find on the lattice a more general power series in fugacity,

$$\rho = \frac{2}{\lambda_T^3}b_1(T)[z + 2b_2(T)z^2 + \cdots]. \tag{12}$$

Although $b_1(T)$ is no longer guaranteed to equal 1, we should find that $b_1(T) \to 1$ in the continuum limit. We use Eq. (12) as the definition for the virial coefficients on the lattice.

In the unitary limit, where the effective range is zero and scattering length is infinite, one finds [22]

$$b_2(T) = 3 \times 2^{-\frac{5}{2}} \approx 0.530. \tag{13}$$

We can compare this with the result for a free Fermi gas, where

$$b_2(T) = -2^{-\frac{5}{2}} \approx -0.177. \tag{14}$$

For zero range but finite scattering length the second virial coefficient becomes

$$b_2(T) = \begin{cases} \dfrac{e^{x^2}}{\sqrt{2}}[1 - \text{erf}(|x|)] - \dfrac{1}{4\sqrt{2}} & \text{for } x < 0, \\ \sqrt{2}e^{\frac{|E_B|}{k_B T}} - \dfrac{e^{x^2}}{\sqrt{2}}[1 - \text{erf}(x)] - \dfrac{1}{4\sqrt{2}} & \text{for } x > 0, \end{cases} \tag{15}$$

where erf is the error function, E_B is the two-particle bound-state energy for positive scattering length, and

$$x = \frac{\lambda_T}{\sqrt{2\pi}a_{\text{scatt}}}. \tag{16}$$

As the effective range goes to zero we have the relation

$$|E_B| = \frac{1}{m a_{\text{scatt}}^2}, \tag{17}$$

and therefore we can write

$$b_2(T) = \begin{cases} \dfrac{e^{x^2}}{\sqrt{2}}[1 - \text{erf}(|x|)] - \dfrac{1}{4\sqrt{2}} & \text{for } x < 0, \\ \sqrt{2}e^{x^2} - \dfrac{e^{x^2}}{\sqrt{2}}[1 - \text{erf}(x)] - \dfrac{1}{4\sqrt{2}} & \text{for } x > 0. \end{cases} \tag{18}$$

See Ref. [23] for a calculation of $b_2(T)$ with realistic interactions, taking into account effective range corrections as well as higher partial waves.

V. BUBBLE CHAIN DIAGRAMS AND THE VIRIAL EXPANSION ON THE LATTICE

The second virial coefficient is determined by two-body interactions. This means that we do not have to rely on simulations to determine $b_2(T)$ on the lattice, but we can extract the second virial coefficient from the lattice regularized bubble chain diagrams. For the neutron propagator we have the diagrams shown in Fig. 5. The bubble diagrams give a contribution to neutron self-energy of the form [15]

$$\Sigma(\vec{q}) = -(1-6h)^2(e^{-C\alpha_t}-1)\frac{1}{L^3L_t} \times \sum_{\vec{p}} \frac{D^{\rm free}(\vec{p}-\vec{q})}{1-(1-6h)^2(e^{-C\alpha_t}-1)B(\vec{p},\mu)}, \quad (19)$$

where

$$B(\vec{p},\mu) = \frac{1}{L^3L_t}\sum_{\vec{k}} \frac{1}{e^{-\mu\alpha_t}e^{-ip_{*0}/2}e^{-ik_{*0}} - 1 + \omega_{p/2+k}} \times \frac{1}{e^{-\mu\alpha_t}e^{-ip_{*0}/2}e^{ik_{*0}} - 1 + \omega_{-p/2+k}}. \quad (20)$$

We use this to compute the full neutron propagator

$$D^{\rm full}(\vec{q}) = \frac{D^{\rm free}(\vec{q})}{1-\Sigma(\vec{q})D^{\rm free}(\vec{q})}. \quad (21)$$

The average number of neutrons is then

$$A = \frac{1}{\beta}\frac{\partial}{\partial\mu}\ln Z_G = 2L^3\left[1 - \frac{e^{(m_N-\mu)\alpha_t}}{L_tL^3}\sum_{\vec{k}} D^{\rm full}(\vec{k})e^{-ik_{*0}}\right]. \quad (22)$$

For the logarithm of the grand canonical partition function, $\ln Z_G$, the lowest nontrivial order in $\rho\lambda_T^3$ is given by the bubble chain diagrams shown in Fig. 6. These give a contribution

$$\ln Z_G - \ln Z_G^{\rm free} = \frac{1}{L_tL^3}\sum_{\vec{p},\vec{q}} \times \frac{-\ln[1-(1-6h)^2(e^{-C\alpha_t}-1)B(\vec{p}+\vec{q},\mu)]D^{\rm free}(\vec{p})D^{\rm free}(\vec{q})}{B(\vec{p}+\vec{q},\mu)}. \quad (23)$$

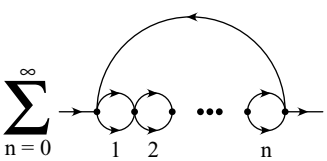

FIG. 5. Bubble chain diagrams contributing to the neutron self-energy.

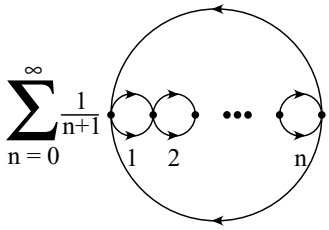

FIG. 6. Bubble chain diagrams contributing to the logarithm of the partition function.

We can now compare these results to the results from simulations and to the virial expansion in the continuum. In Fig. 7 we plot the density versus fugacity at $T = 4$ MeV for scattering lengths $a_{\rm scatt} = \pm 18.7$ fm. We show data for a free Fermi gas on the lattice, bubble chain calculations, and full simulation results. We also plot first- and second-order virial results using $b_1(T) = 1.27$, which we obtained by fitting the bubble chain data at very small fugacity. The results for the free Fermi gas on the lattice agree with the second-order virial results with $b_2(T) = -0.177$. The bubble chain and full simulation results for $a_{\rm scatt} = \pm 18.70$ fm are not very far from the second-order curve for $b_2(T) = 0.530$. However, the results for -18.70 fm and $+18.70$ fm both lie above the second-order virial curve, rather than one on either side.

In Fig. 8 we plot the density versus fugacity at $T = 3$ MeV and virial curves with $b_1(T) = 1.28$. In Fig. 9 we plot the density versus fugacity at $T = 2$ MeV and virial curves with $b_1(T) = 1.22$. Again we determined $b_1(T)$ by fitting the bubble chain data at very small fugacity. The free Fermi gas results on the lattice at $T = 3$ and 2 MeV match the second-order virial results at $b_2(T) = -0.177$. But we find the same problem for the bubble chain and full simulation results. The results for $a_{\rm scatt} = -18.70$ fm and $+18.70$ fm both lie above the

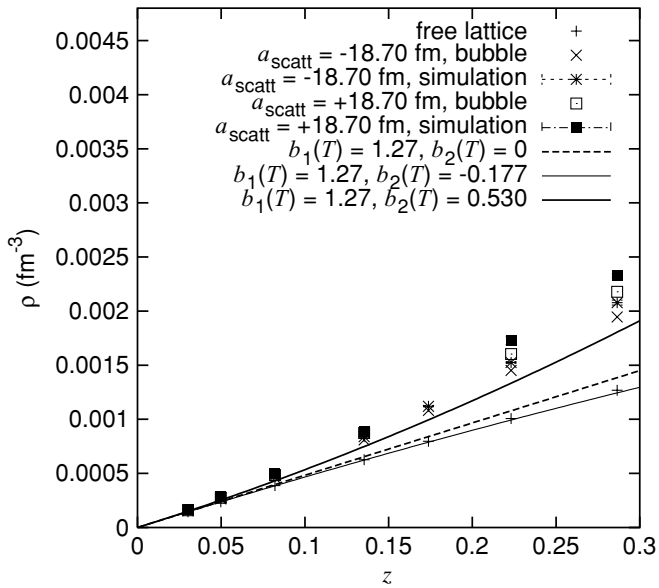

FIG. 7. Density versus fugacity at $T = 4$ MeV for scattering lengths $a_{\rm scatt} = \pm 18.70$ fm. We show comparisons with the first- and second-order virial expansion.

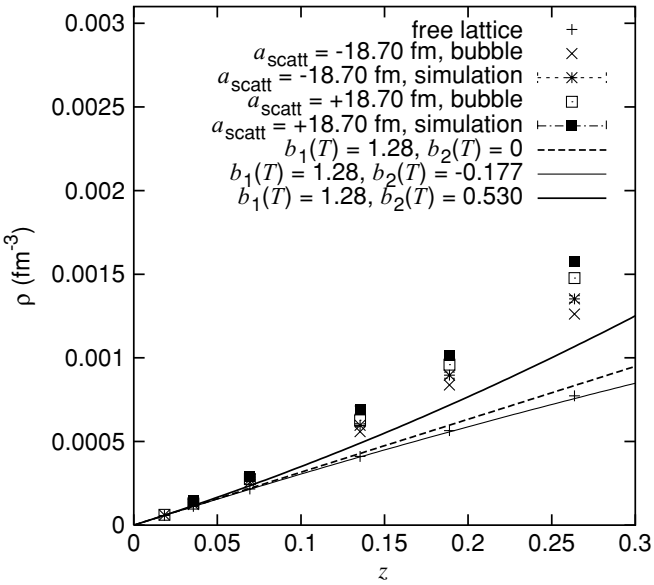

FIG. 8. Density versus fugacity at $T = 3$ MeV for scattering lengths $a_{\text{scatt}} = \pm 18.70$ fm. We show comparisons with the first- and second-order virial expansion.

second-order virial curve for $b_2(T) = 0.530$. Furthermore, the deviation appears to be worse at colder temperatures.

VI. LATTICE VIRIAL COEFFICIENTS

We use the bubble chain expansion to compute $b_2(T)$ on the lattice for the various coupling strengths and temperatures mentioned above. The specific procedure we use is as follows. We first compute the free Fermi gas density on the lattice and

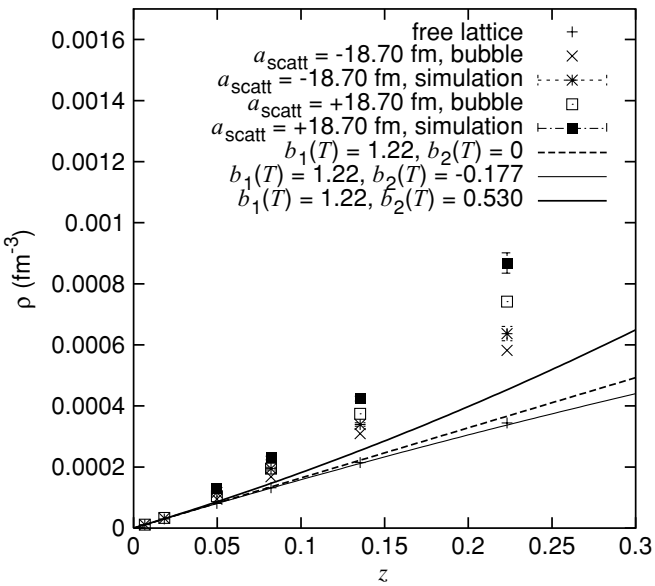

FIG. 9. Density versus fugacity at $T = 2$ MeV for scattering lengths $a_{\text{scatt}} = \pm 18.70$ fm. We show comparisons with the first- and second-order virial expansion.

TABLE III. $b_1(T)$ on the lattice.

T(MeV)	L	$b_1(T)$
4	5	1.273
3	6	1.282
2	6	1.221
1.5	7	1.160
1	8	1.091
0.667	9	1.053
0.5	10	1.038

use the relation

$$\rho^{\text{free}} \approx \frac{2}{\lambda_T^3} b_1(T)(z - 2 \times 2^{-\frac{5}{2}} z^2) \tag{24}$$

to determine $b_1(T)$. This can be measured at any small fugacity, and we choose $z = e^{-5} \approx 0.0067$ or $\mu = -5k_BT$. In Table II we show results for $b_1(T)$ for a range of temperatures. We have taken the lattice volume to be large enough so that the finite volume error is 0.1% or less, and the values for L are shown in Table III.

As the temperature decreases we see that $b_1(T) \to 1$. This is expected because at fixed lattice spacing the system moves closer to the continuum limit as we decrease the temperature.

With the same chemical potential and lattice volumes, we compute the density in the bubble chain approximation and determine $b_2(T)$ using the relation

$$\rho^{\text{bubble}} \approx \frac{2}{\lambda_T^3} b_1(T)[z + 2b_2(T)z^2]. \tag{25}$$

The results for $b_2(T)$ for the various coupling strengths are shown in Table IV. For each pair shown the lattice result is on the left and the continuum result is on the right.

We see that the lattice virial coefficients are larger than the continuum values. Also as we decrease the temperature at

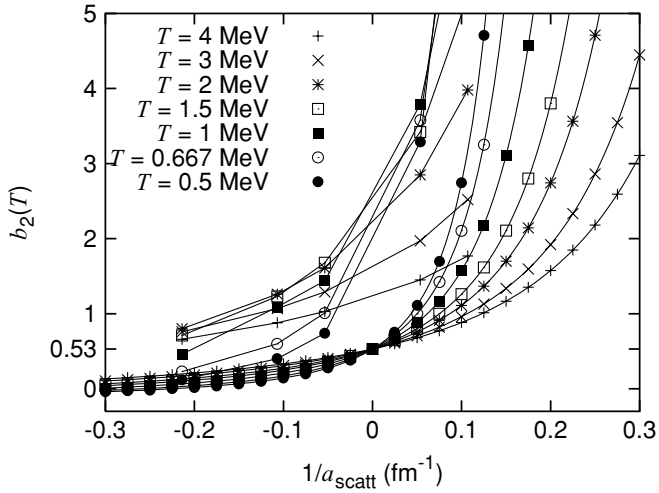

FIG. 10. Plot of second virial coefficient as function of inverse scattering length for various temperatures. The smooth curves are the continuum results, and the points with interpolating lines are the lattice results.

TABLE IV. Second virial coefficient $b_2(T)$ for different scattering lengths $a_{\rm scatt}$ as calculated on the lattice (first column) and in the continuum limit (second column).

$a_{\rm scatt}$ (fm)	−4.675		−9.35		−18.70		+18.70		+9.35	
C (10^{-4} MeV^{-2})	−1.028		−1.108		−1.153		−1.257		−1.318	
$T = 4$ MeV	0.66	0.198	0.88	0.322	1.03	0.411	1.45	0.692	1.77	0.917
$T = 3$ MeV	0.76	0.170	1.07	0.299	1.29	0.396	1.97	0.722	2.52	1.004
$T = 2$ MeV	0.80	0.131	1.26	0.263	1.61	0.371	2.85	0.776	3.98	1.176
$T = 1.5$ MeV	0.71	0.103	1.23	0.237	1.68	0.352	3.42	0.825	5.22	1.350
$T = 1$ MeV	0.46	0.066	1.09	0.198	1.44	0.322	3.79	0.917	6.85	1.720
$T = 0.667$ MeV	0.23	0.031	0.60	0.159	1.01	0.289	3.58	1.047	8.01	2.368
$T = 0.5$ MeV	0.12	0.008	0.40	0.131	0.74	0.263	3.29	1.176	8.82	3.167

fixed scattering length, the deviation in $b_2(T)$ first increases before eventually decreasing.

VII. DISCUSSION

In Fig. 10 we plot $b_2(T)$ versus inverse scattering length for a range of temperatures. The smooth curves are the continuum results given in Eq. (18), and the points with interpolating guide lines are the lattice results from Table IV. For the continuum curves we see that the value of b_2 at infinite scattering length remains fixed at $3 \times 2^{-\frac{5}{2}} \approx 0.530$. However, as the temperature decreases, the slope as a function of inverse scattering length steepens. The functional dependence of b_2 on $a_{\rm scatt}$ and T is roughly

$$b_2 \sim e^{x^2} = e^{\frac{1}{a_{\rm scatt}^2 m_N T}}. \tag{26}$$

We observe that the lattice virial curves are actually not very different from the continuum virial curves. However, they are shifted to the left slightly as a function of the inverse scattering length. The large slope together with this leftward shift is responsible for the large lattice virial coefficients. This is seen even more clearly in Figs. 11 and 12, where we show the continuum and lattice virial results at temperatures $T = 1$ and 0.5 MeV along with shifted lattice results so that b_2 equals 0.530 at infinite scattering length. We see that the shifted curves appears to match the continuum results relatively well. The required shift as a function of temperature appears to decrease with temperature, though the exact dependence requires further study.

Physically the large error in the second virial coefficient is directly related to singularities in the sum over particle-particle bubble diagrams because of either true bound states for positive scattering length or zero-energy resonances in the unitary limit. Although the singularities are completely integrable at nonzero temperature, on the lattice the momentum integrals are finite sums that can be very sensitive to small perturbations. The obvious way to address this problem, aside from working at a much smaller lattice spacing, is to use an improved lattice action, one that includes more than simple nearest-neighbor hopping terms for the kinetic energy as well as higher-order corrections to the interaction. We are currently investigating improved actions, but this is not an easy task and not all improved operators maintain the positivity of the euclidean action.

We propose that even with an unimproved action one can improve the scaling behavior of the data by tuning the coefficient C to give the correct physical value of the second virial coefficient $b_2(T)$ for each desired simulation

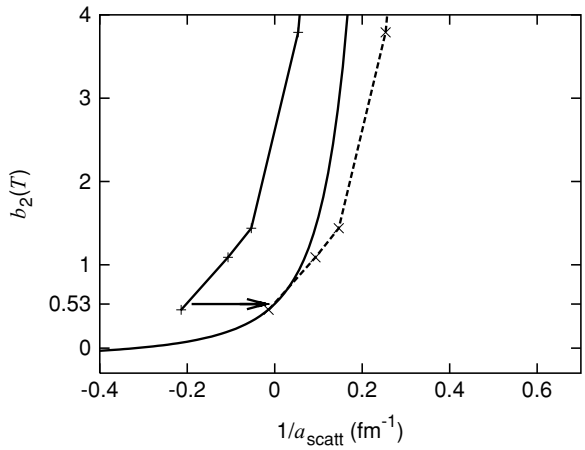

FIG. 11. Plot of continuum and lattice virial results for $T = 1$ MeV. We also show the lattice results shifted horizontally so that b_2 equals 0.530 at infinite scattering length.

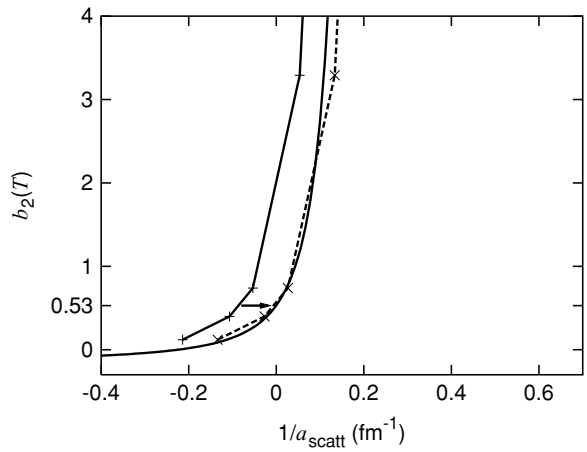

FIG. 12. Plot of continuum and lattice virial results for $T = 0.5$ MeV. We also show the lattice results shifted horizontally so that b_2 equals 0.530 at infinite scattering length.

temperature. Because $b_2(T)$ on the lattice is easily calculated this is not much of an added burden. This procedure coincides with the standard approach of fixing the zero temperature scattering length in the limit that the lattice spacing goes to zero or as $T \to 0$ at fixed lattice spacing. Fixing $b_2(T)$ will obviously improve the scaling behavior at low density. Whether it will also improve the data in the degenerate regime is not a priori clear and this question is the focus of our companion article.

ACKNOWLEDGMENTS

This work is supported in part by the U.S. Department of Energy grants DE-FG-88ER40388 (T.S.) and DE-FG02-04ER41335 (D.L.).

[1] C. J. Pethick and D. G. Ravenhall, Annu. Rev. Nucl. Part. Sci. **45**, 429 (1995).
[2] K. M. O'Hara, S. L. Hemmer, M. E. Gehm, S. R. Granade, and J. E. Thomas, Science **298**, 2179 (2002).
[3] S. Gupta, Z. Hadzibabic, M. W. Zwierlein, C. A. Stan, K. Dieckmann, C. H. Schunck, E. G. M. van Kempen, B. J. Verhaar, and W. Ketterle, Science **300**, 1723 (2003).
[4] C. A. Regal and D. S. Jin, Phys. Rev. Lett. **90**, 230404 (2003).
[5] T. Bourdel, J. Cubizolles, L. Khaykovich, K. M. F. Magalhaes, S. J. J. M. F. Kokkelmans, G. V. Shlyapnikov, and C. Salomon, Phys. Rev. Lett. **91**, 020402 (2003).
[6] M. E. Gehm, S. L. Hemmer, S. R. Granade, K. M. O'Hara, and J. E. Thomas, Phys. Rev. A **68**, 011401(R) (2003).
[7] J. Carlson, J. Morales Jr., V. R. Pandharipande, and D. G. Ravenhall, Phys. Rev. C **68**, 025802 (2003).
[8] J. Carlson, S. Y. Chang, V. R. Pandharipande, and K. E. Schmidt, Phys. Rev. Lett. **91**, 050401 (2003).
[9] S. Y. Chang *et al*., Nucl. Phys. **A746**, 215 (2004).
[10] F. Pederiva, A. Sarsa, K. E. Schmidt, and S. Fantoni, Nucl. Phys. **A742**, 255 (2004).
[11] H. M. Müller and R. Seki, in *Nuclear physics with effective field theory. Proceedings, Joint Caltech/INT Workshop, Pasadena, USA, February 26–27, 1998* (World Scientific, Singapore, 1998), pp. 191–203.
[12] H. M. Müller, S. E. Koonin, R. Seki, and U. van Kolck, Phys. Rev. C **61**, 044320 (2000).
[13] T. Abe, R. Seki, and A. N. Kocharian, Phys. Rev. C **70**, 014315 (2004); erratum-*ibid*. **71**, 059902 (2005).
[14] D. Lee, B. Borasoy, and T. Schaefer, Phys. Rev. C **70**, 014007 (2004).
[15] D. Lee and T. Schafer, Phys. Rev. C **72**, 024006 (2005).
[16] M. Wingate (2005), cond-mat/0502372.
[17] A. Bulgac, J. E. Drut, and P. Magierski (2005), cond-mat/0505374.
[18] R. Seki and U. van Kolck (2005), nucl-th/0509094.
[19] M. Lüscher, Commun. Math. Phys. **105**, 153 (1986).
[20] S. R. Beane, P. F. Bedaque, A. Parreno, and M. J. Savage, Phys. Lett. **B585**, 106 (2004).
[21] S. Duane, A. D. Kennedy, B. J. Pendleton, and D. Roweth, Phys. Lett. **B195**, 216 (1987).
[22] T.-L. Ho and E. J. Mueller, Phys. Rev. Lett. **92**, 160404 (2004).
[23] C. J. Horowitz and A. Schwenk (2005), nucl-th/0507064.